Journal of Power Sources 206 (2012) 59–69

Contents lists available at SciVerse ScienceDirect

Journal of Power Sources

journal homepage: www.elsevier.com/locate/jpowsour

Thermomechanical, transport and anodic properties of perovskite-type $(La_{0.75}Sr_{0.25})_{0.95}Cr_{1-x}Fe_xO_{3-\delta}$

M.F. Lü [a], E.V. Tsipis [b], J.C. Waerenborgh [b], A.A. Yaremchenko [a], V.A. Kolotygin [a], S. Bredikhin [c], V.V. Kharton [a,*]

[a] Department of Ceramics and Glass Engineering, CICECO, University of Aveiro, 3810-193 Aveiro, Portugal
[b] Chemistry Department, Instituto Tecnológico e Nuclear, CFMC-UL, EN 10, 2686-953 Sacavém, Portugal
[c] Institute of Solid State Physics RAS, Institutskaya 2, 142432 Chernogolovka, Moscow Region, Russia

ARTICLE INFO

Article history:
Received 29 September 2011
Received in revised form 12 January 2012
Accepted 15 January 2012
Available online 23 January 2012

Keywords:
SOFC anode
Lanthanum chromite–ferrite
Mixed conductivity
Mössbauer spectroscopy
Dilatometry
Electrode polarization

ABSTRACT

Effects of iron doping on the functional properties of (La,Sr)CrO_3-based electrode materials have been appraised in a range of conditions relevant for SOFCs and other electrochemical applications. Mössbauer spectroscopy of perovskite-type $(La_{0.75}Sr_{0.25})_{0.95}Cr_{1-x}Fe_xO_{3-\delta}$ (x = 0.3–0.4), combined with thermogravimetry and X-ray diffraction, shows that the prevailing oxidation state of iron cations in both oxidizing and reducing atmospheres remains 3+. The redox behavior and transport properties are, therefore, essentially governed by $Cr^{3+/4+}$ couple, leading to dominant p-type electronic conduction in the oxygen partial pressure range from 0.5 down to 10^{-20} atm at 973–1223 K. The total conductivity and Seebeck coefficient variations indicate that the electronic transport decreases with iron additions as the hole concentration and mobility become lower. The partial ionic conductivity estimated from the steady-state oxygen permeability under air/H_2–H_2O–N_2 gradients is 0.05–0.08 S cm^{-1} at 1223 K and $p(O_2) = 10^{-17}$ atm, and increases with x due to rising oxygen deficiency. A similar tendency was observed for chemical expansion studied by the controlled-atmosphere dilatometry, whereas the average thermal expansion coefficients are almost independent of x and vary from 11.1–11.3 × 10^{-6} K^{-1} in air down to 10.3–10.5 × 10^{-6} K^{-1} in CO–CO_2 at 350–1370 K. The electrochemical activity of porous $(La_{0.75}Sr_{0.25})_{0.95}Cr_{0.7}Fe_{0.3}O_{3-\delta}$ anodes with $Ce_{0.8}Gd_{0.2}O_{2-\delta}$ interlayers, applied onto $LaGaO_3$-based solid electrolyte, is higher compared to $(La_{0.75}Sr_{0.25})_{0.95}Cr_{0.5}Mn_{0.5}O_{3-\delta}$ when no metallic current-collecting layers are used. Increasing iron content lowers the electrode performance in wet H_2-containing atmospheres, in correlation with electronic conduction.

1. Introduction

Energy-related systems based on solid oxide fuel cells (SOFCs) and electrolysis cells (SOECs) offer important potential advantages due to a high efficiency, environmental safety, fuel flexibility including the prospects to directly utilize hydrocarbons and gasified coal, and possibility to recover exhaust heat [1–7]. Significant efforts are focused on the developments of oxide electrode materials stable in both oxidizing and reducing environments, in order to reduce costs of the electrochemical devices and to suppress degradation phenomena, such as coking and sulfur poisoning of the electrodes operating in fuel atmospheres. These problems are well known for the conventional SOFC anodes of Ni-containing cermets, which also degrade due to large volume changes on redox cycling and to sintering during SOFC operation [3–9]. At the same time, alternative oxide electrode compositions based on perovskite-related titanates and chromites stable in relatively wide ranges of the oxygen partial pressures, $p(O_2)$, possess usually a number of other functional disadvantages, primarily a worse electrochemical activity and lower electronic transport compared to the cermets. A very promising combination of properties was recently reported for perovskite-type $(La_{0.75}Sr_{0.25})_{1-y}Cr_{0.5}Mn_{0.5}O_{3-\delta}$ (y = 0–0.05) [3,4,10–12]. In these perovskites (LSCM), the presence of rigid CrO_6 octahedra in the crystal structure enables its stabilization down to low oxygen chemical potentials necessary for the SOFC anode operation, while moderate acceptor-type doping is necessary to improve electronic and ionic conduction. Nevertheless, the electrochemical performance of LSCM anodes without any additional components is essentially limited by the electronic transport, leading to rather high overpotentials; the incorporation of metals (e.g., Ni or Cu) and/or electrocatalytically active additives (e.g., $CeO_{2-\delta}$) decreases

* Corresponding author. Tel.: +351 234 370263; fax: +351 234 425300.
E-mail address: kharton@ua.pt (V.V. Kharton).

0378-7753/$ – see front matter © 2012 Elsevier B.V. All rights reserved.
doi:10.1016/j.jpowsour.2012.01.100

Table 1
Properties of $(La_{0.75}Sr_{0.25})_{0.95}$ $Cr_{1-x}Fe_xO_{3-\delta}$ ceramics.

x	Unit cell parameters[a], Å	Relative density, %	Average thermal expansion coefficients[b]			Activation energy for total conductivity in air	
			Atmosphere	T, K	TEC × 10^6, K^{-1} (±0.1 × 10^6)	T, K	E_a, kJ mol^{-1}
0.3	a = 5.5136(1)	95.2	Air	470–1220	11.3	300–470	23 ± 2
	c = 13.3514(3)		CO–CO_2[c]	350–1370	10.3	470–1290	15.1 ± 0.1
0.4	a = 5.5170(1)	92.5	Air	470–1250	11.1	300–570	13.9 ± 0.2
	c = 13.3597(3)		CO–CO_2	350–1370	10.5	580–1290	16.9 ± 0.1

[a] Space group $R\bar{3}c$, hexagonal settings.
[b] The average TECs were calculated from the dilatometric data collected on cooling after equilibration in the given atmosphere at high temperatures.
[c] The oxygen partial pressure in the CO–CO_2 gas mixture supplied in the dilatometer was 3×10^{-20} atm at 923 K and 2×10^{-12} atm at 1223 K.

electrode resistance [10–12]. Notice that introducing a ceria-based buffer layer between lanthanum gallate-based electrolyte and $La_{0.75}Sr_{0.25}Cr_{0.5}Mn_{0.5}O_{3-\delta}$ electrode enables also to suppress diffusion of Cr and Mn cations into the solid-electrolyte surface layers [11].

Doping of acceptor-substituted $LaCrO_{3-\delta}$ with iron may further enhance electrode performance [4,5]. For example, a lower polarization resistance with respect to LSCM was reported for the electrodes made of its Fe-containing analog, $La_{0.75}Sr_{0.25}Cr_{0.5}Fe_{0.5}O_{3-\delta}$ [4]. The electrochemical cells with $La_{0.75}Sr_{0.25}Cr_{0.5}Fe_{0.5}O_{3-\delta}$ electrodes and (La,Sr)(Ga,Mg)$O_{3-\delta}$ (LSGM) solid electrolyte exhibit however a higher series resistance, presumably due to stronger reactivity of the materials in comparison with LSCM|LSGM cells [4]. An excellent performance was observed for the composite anodes made of perovskite-type $LaSr_2Fe_2CrO_{9-\delta}$ and gadolinia-doped ceria (CGO), with an additional CGO interlayer applied between the electrode and LSGM electrolyte [5]. On the other hand, literature data on phase stability of (La,Sr)(Cr,Fe)$O_{3-\delta}$ in reducing atmospheres are still quite contradictory [3–6,13], whereas information on thermomechanical and transport properties of these perovskites is very scarce.

The present work is focused on the evaluation of anode behavior and other functional properties of $(La_{0.75}Sr_{0.25})_{0.95}Cr_{1-x}Fe_xO_{3-\delta}$ (x = 0.3–0.4). The concentration of iron cations in this model system was selected lower than that in $La_{0.75}Sr_{0.25}Cr_{0.5}Fe_{0.5}O_{3-\delta}$ [4] and $LaSr_2Fe_2CrO_{9-\delta}$ [5], thus making it possible to expect a moderate enlargement of the perovskite phase stability domain under reducing conditions due to higher fraction of iron–oxygen polyhedra surrounded exclusively by the CrO_6 octahedra. Emphasis is given to the properties important for practical application, namely thermal and chemical expansion, electronic conductivity, oxygen permeability, and electrode behavior. In order to assess phase stability and electronic transport mechanisms, Mössbauer spectroscopy and Seebeck coefficient measurements were also employed. The anodic overpotentials of porous $(La_{0.75}Sr_{0.25})_{0.95}Cr_{1-x}Fe_xO_{3-\delta}$ electrodes applied onto LSGM with CGO interlayer are compared to those of LSCM and (La,Sr)(Mn,Ti)$O_{3-\delta}$, which were studied under similar conditions and partly reported elsewhere [12,14].

2. Experimental

Single-phase powders of $(La_{0.75}Sr_{0.25})_{0.95}Cr_{1-x}Fe_xO_{3-\delta}$ were prepared by the glycine–nitrate process, a self-combustion technique utilizing nitrates of metal components as an oxidant and glycine as a fuel and chelating agent [15]. The obtained foam-like powders were annealed in air at 1273 K for 8 h in order to remove organic residuals, and then grinded. Gas-tight ceramic samples for the measurements of total conductivity, thermal expansion and oxygen permeability were uniaxially compacted at 50–150 MPa and sintered in air at 1973 for 5 h, with subsequent slow cooling (2–4 K min^{-1}) to achieve equilibrium with atmospheric oxygen at low temperatures. The density of ceramic materials was in the range 92–95% of their theoretical density calculated from X-ray diffraction (XRD) results, Table 1. The powdered samples used for XRD, Mössbauer spectroscopy and thermogravimetric analysis (TGA), were obtained by grinding of sintered ceramics. Additional series of samples used for the studies of phase composition and iron states at elevated temperatures, were also annealed at 1223 K in air and in a flowing H_2–H_2O–N_2 mixture with $p(O_2) = 10^{-18}$ atm for 44 h, and then quenched.

Materials characterization included XRD (Rigaku D/Max-B and PANalytical X'Pert Pro diffractometers), scanning electron microscopy coupled with energy dispersive spectroscopy (SEM/EDS, Hitachi S-4100/SU-70), controlled-atmosphere dilatometry (Linseis L70/2001), TGA (Setaram SetSys 16/18), inductively coupled plasma (ICP) spectroscopic analysis (Jobin Yvon 70 plus), measurements of total conductivity (four-probe DC) and Seebeck coefficient as a function of temperature and oxygen partial pressure, and determination of steady-state oxygen permeation fluxes under air/H_2–H_2O–N_2 gradients. Detailed description of the experimental procedures and equipment was published elsewhere [12,14,16–21]. For the measurements of electrical properties, the criteria for equilibration of a sample after a change in either oxygen activity or temperature included the relaxation rates of the conductivity and Seebeck coefficients less than 0.04% min^{-1} and 0.001 μV K^{-1} min^{-1}, respectively; the equilibration times varied from 2–4 h up to 80 h.

Mössbauer transmission spectra were collected at room temperature and 4 K using a conventional constant-acceleration spectrometer and a 25 mCi ^{57}Co source in a Rh matrix. The velocity scale was calibrated using α-Fe foil. The absorbers were obtained by pressing the powdered samples into perspex holders. Isomer shifts (IS, Table 2) are related to metallic α-Fe at room temperature. The 4 K spectra were collected using a JANIS bath cryostat, model SVT-400, with the sample immersed in liquid He. The spectra were fitted to Lorentzian lines using a non-linear least-squares method [20]. In the course of refinement procedure, the relative areas and line widths of both peaks in a quadrupole doublet and of the symmetrical peaks constituting a magnetic sextet (i.e., peaks 1–6, 2–5 and 3–4) were constrained to remain equal. The distribution of magnetic splittings was fitted according to the histogram method [22].

The steady-state anode polarization experiments were performed by the 3-electrode technique using the electrochemical cells comprising symmetrical working (WE) and counter (CE) electrodes made of porous (La,Sr)(Cr,Fe)$O_{3-\delta}$ and Pt, respectively, $Ce_{0.8}Gd_{0.2}O_{2-\delta}$ interlayers, $(La_{0.9}Sr_{0.1})_{0.98}Ga_{0.8}Mg_{0.2}O_{3-\delta}$ solid electrolyte membranes, porous Pt reference electrodes (REs), and Pt gauze current collectors. The cell configuration, fabrication conditions and measuring procedures were all identical to those described in Ref. [12]; processing and functional properties of $(La_{0.9}Sr_{0.1})_{0.98}Ga_{0.8}Mg_{0.2}O_{3-\delta}$ (LSGM) electrolyte ceramics were reported in Ref. [19]. Prior to the WE deposition, as-prepared $(La_{0.75}Sr_{0.25})_{0.95}Cr_{1-x}Fe_xO_{3-\delta}$ powders were annealed in air at

Table 2
Parameters[a] estimated from the Mössbauer spectra of $(La_{0.75}Sr_{0.25})_{0.95}Cr_{1-x}Fe_xO_{3-\delta}$ equilibrated in air and in reducing atmosphere.

x	Equilibration conditions	CN	Measurement temperature, K	IS (mm s^{-1})	QS, 2ε (mm s^{-1})	B_{hf} (T)	I (%)
0.3	$p(O_2)$ = 0.21 atm, 295 K	6	295	0.35	0.34	–	100
			4	0.46	−0.02	46.0	100
0.4	$p(O_2)$ = 0.21 atm, 295 K	6	295	0.35	0.31	–	100
			4	0.48	−0.02	48.0	100
0.3	$p(O_2) = 10^{-18}$ atm, 1223 K	6	295	0.36	0.36	–	29
		5		0.27	1.07	–	71
0.4	$p(O_2) = 10^{-18}$ atm, 1223 K	6	295	0.36	0.34	–	42
		5		0.28	1.06	–	58

[a] CN, IS, QS, $2\varepsilon = (e^2V_{ZZ}Q/4)(3\cos^2\theta - 1)$, B_{hf} and I are the coordination number of trivalent iron, isomer shift relative to metallic α-Fe at 295 K, quadrupole shift, magnetic hyperfine field and relative area, respectively. The average B_{hf} values of magnetic sextet distributions are given. Estimated errors are ≤0.2 T for B_{hf}, <2% for I, and ≤0.02 mm s^{-1} for the other parameters. CN is the coordination number of iron cations in the perovskite lattice.

1473 K during 10 h in order to avoid local inhomogeneities, phase separation and excessive sintering of the porous layers; these conditions were selected on the basis of preliminary tests involving various thermal treatments, XRD and SEM/EDS. Then the (La,Sr)(Cr,Fe)$O_{3-\delta}$ electrodes were applied onto CGO|LSGM half-cells and sintered at 1473 K for 10 h in air. After fabrication of CE and RE, assembling of the setup and sealing, the anodes were equilibrated at 1073 K in 10%H_2–90%N_2 atmosphere (flow rate of 3 l h^{-1}) during 15–25 h before starting the measurements. The polarization tests were carried out in the galvanostatic mode using a PGSTAT302 Autolab instrument at 873–1073 K in flowing wet 10%H_2–N_2 gas mixture (3 l h^{-1}) where the oxygen chemical potential was continuously controlled by an electrochemical oxygen sensor. The ohmic (R) and polarization (R_η) resistances were determined from the impedance spectra collected in the frequency range from 10 mHz to 1 MHz (AC signal amplitude of 3 mA). The relaxation times after a change in the working electrode potential or temperature were 1–8 h. The as-prepared and tested electrodes were examined by XRD and SEM/EDS in order to reveal possible structural and microstructural alterations.

3. Results and discussion

3.1. Structural and microstructural characterization

XRD analysis confirmed that as-prepared $(La_{0.75}Sr_{0.25})_{0.95}Cr_{1-x}Fe_xO_{3-\delta}$ powders and ceramics are single-phase, as expected (Fig. 1). The crystal structure under oxidizing conditions was identified as rhombohedrally distorted perovskite (space group $R\bar{3}c$); the unit cell parameters are listed in Table 1. Note that the rhombohedral symmetry was earlier reported for $LaSr_2(Fe,Cr)O_{8+\delta}$ [23], whereas $La_{0.75}Sr_{0.25}Cr_{0.5}Fe_{0.5}O_3$ is orthorhombic [24]. Compared to the latter compound, the higher symmetry of oxidized $(La_{0.75}Sr_{0.25})_{0.95}Cr_{1-x}Fe_xO_3$ (x = 0.3–0.4) originates from the higher concentration of Cr^{3+}/Cr^{4+} cations having smaller radii with respect to Fe^{3+}/Fe^{4+} [25], thus increasing the perovskite tolerance factor. Moreover, in accordance with the data on electronic transport and Mössbauer spectra discussed below, the average oxidation state of chromium cations is higher than that of iron, again decreasing the average size of B-site cations in the ABO_3 perovskite structure. Consequently, reduction in H_2-containing atmospheres leads to a larger radius of these cations and to a lower symmetry. Rietveld refinement of the XRD patterns of reduced $(La_{0.75}Sr_{0.25})_{0.95}Cr_{1-x}Fe_xO_{3-\delta}$ (Fig. 1) showed the formation of orthorhombic perovskite structure, space group *Pbnm*. At the same time, no traces of metallic iron or other secondary phases were detected, in agreement with Mössbauer spectroscopy. This confirms phase stability of the title perovskites in a wide $p(O_2)$ range necessary for the SOFC anode applications, although the "rhombohedral ↔ orthorhombic" transition may contribute to chemically induced strains on redox cycling.

EDS/SEM inspection of the dense ceramics and porous electrodes revealed an absence of compositional inhomogeneities and quite uniform grain size. The cation composition of selected samples was also verified by the ICP spectroscopy. Typical microstructures are shown in Fig. 2. The electrodes were found to possess a sufficient porosity and a relatively high surface area, ensuring gas penetration and facile surface-exchange processes. The average grain diameter in the electrode layers varied in the range 0.5–2 μm. No exfoliation or visible reaction traces between $(La_{0.75}Sr_{0.25})_{0.95}Cr_{1-x}Fe_xO_{3-\delta}$ and CGO interlayer were observed (Fig. 2D). The electrochemical tests during over 150 h did not result in significant changes of the electrode grain size.

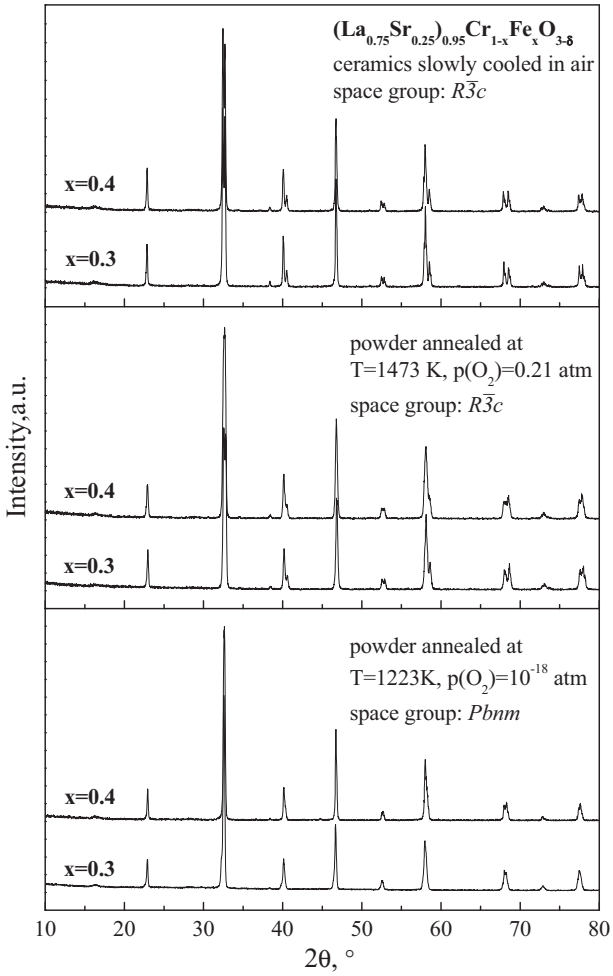

Fig. 1. XRD patterns of $(La_{0.75}Sr_{0.25})_{0.95}Cr_{1-x}Fe_xO_{3-\delta}$ (x = 0.3, 0.4) after sintering in air at 1973 K, annealing in air at 1473 K and subsequent reduction in H_2–H_2O–N_2 atmosphere at 1223 K.

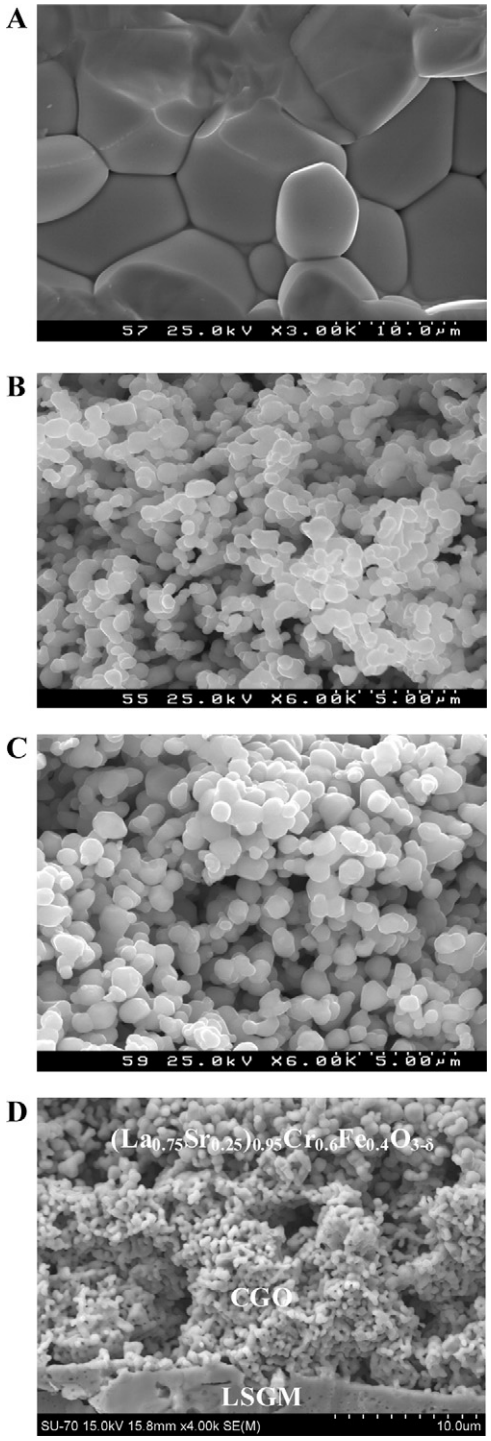

Fig. 2. SEM micrographs of fractured $(La_{0.75}Sr_{0.25})_{0.95}Cr_{0.6}Fe_{0.4}O_{3-\delta}$ ceramics (A), top-view of as-prepared porous electrodes of $(La_{0.75}Sr_{0.25})_{0.95}Cr_{0.7}Fe_{0.3}O_{3-\delta}$ (B) and $(La_{0.75}Sr_{0.25})_{0.95}Cr_{0.6}Fe_{0.4}O_{3-\delta}$ (C), and fractured $(La_{0.75}Sr_{0.25})_{0.95}Cr_{0.6}Fe_{0.4}O_{3-\delta}$ electrode applied onto CGO|LSGM after electrochemical measurements in H_2-containing atmosphere (D).

3.2. Defect formation in oxidized $(La_{0.75}Sr_{0.25})_{0.95}Cr_{1-x}Fe_xO_{3-\delta}$

The Mössbauer spectra of $(La_{0.75}Sr_{0.25})_{0.95}Cr_{1-x}Fe_xO_{3-\delta}$, equilibrated with atmospheric oxygen down to room temperature, are shown in Figs. 3 and 4. The room-temperature spectra (Fig. 4, top) can be adequately described by a quadrupole doublet with isomer shifts typical for octahedrally coordinated Fe^{3+} in oxide phases, Table 2 (e.g., [26–28] and references cited). At 4.2 K, below the

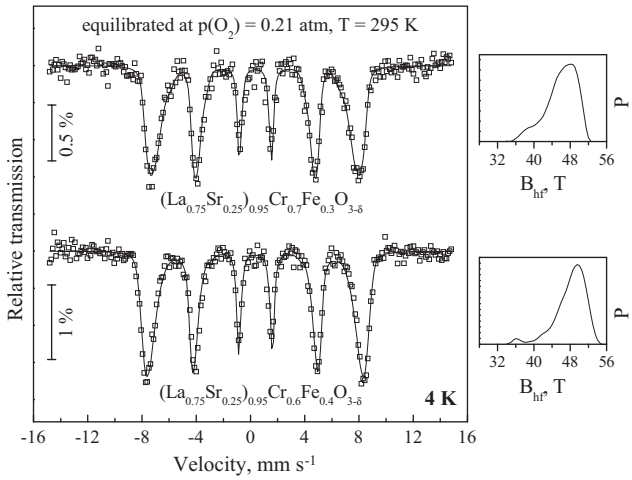

Fig. 3. Mössbauer spectra of oxidized $(La_{0.75}Sr_{0.25})_{0.95}Cr_{1-x}Fe_xO_{3-\delta}$, collected at 4 K. The lines plotted over the experimental points are the distributions of magnetic sextets. Insets show the probability distribution of the magnetic hyperfine fields.

magnetic transition point, a distribution of magnetic sextets is observed (Fig. 3). The estimated IS and the average magnetic hyperfine field (B_{hf}) indicate that six-fold coordinated Fe^{3+} is the predominant state of iron cations. The distribution originates hence from the so-called chemical disorder, i.e., the presence of different cations in the nearest coordination spheres of iron (Cr^{3+}, Cr^{4+} and Fe^{3+} in the B sublattice, and La^{3+} and Sr^{2+} in the A sites). The

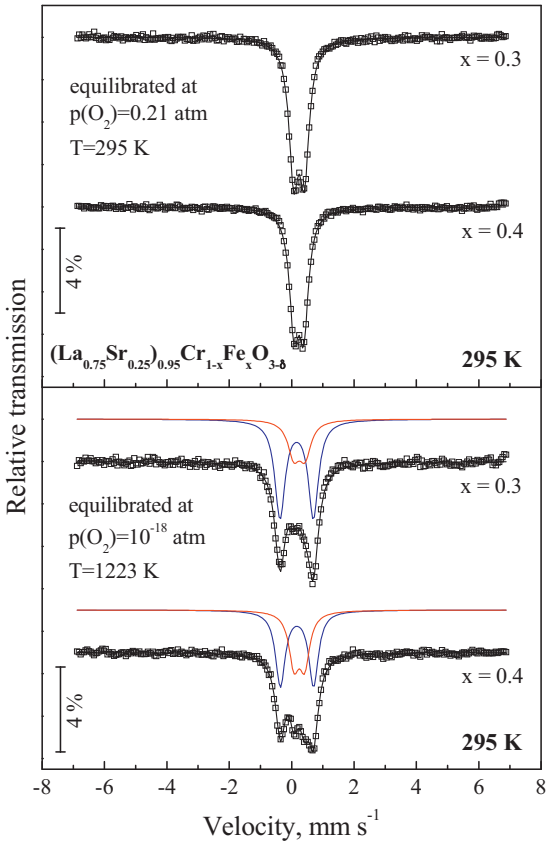

Fig. 4. Room-temperature Mössbauer spectra of $(La_{0.75}Sr_{0.25})_{0.95}Cr_{1-x}Fe_xO_{3-\delta}$, equilibrated in atmospheric air down to room temperature (top) and reduced in flowing H_2–N_2–H_2O gas mixture at 1223 K and $p(O_2) = 10^{-18}$ atm during 44 h (bottom). The lines plotted over the experimental points are the quadrupole doublet or the sum of two doublets shown shifted for clarity.

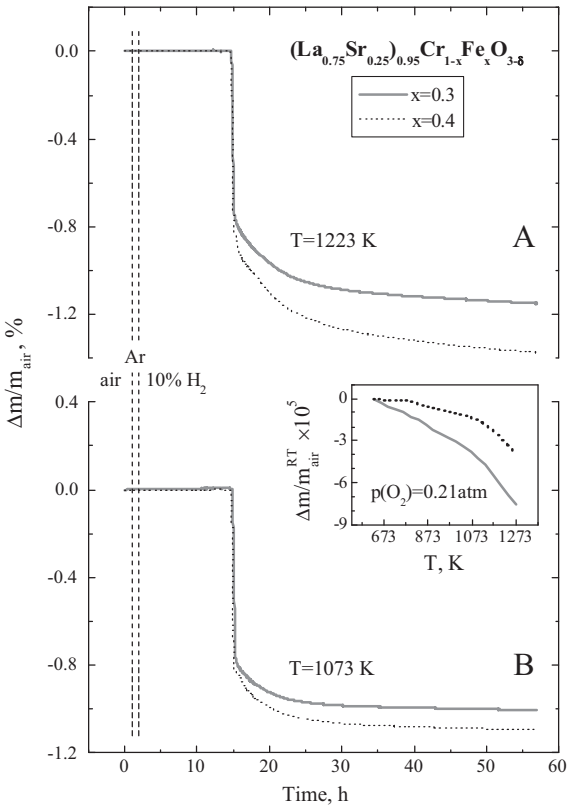

Fig. 5. Relative weight changes in $(La_{0.75}Sr_{0.25})_{0.95}Cr_{1-x}Fe_xO_{3-\delta}$, measured by TGA on reduction in flowing dry 10%H_2–90%N_2 gas mixture at 1223 K (A) and 1073 K (B). Inset shows the weight changes in atmospheric air with respect to room temperature. Dashed vertical lines correspond to the atmosphere changes from air to flowing Ar and then to 10%H_2–90%N_2.

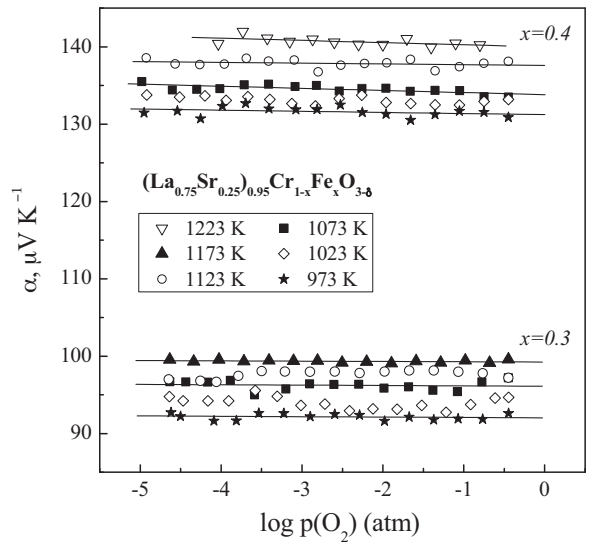

Fig. 6. Oxygen partial pressure dependencies of Seebeck coefficient $(La_{0.75}Sr_{0.25})_{0.95}Cr_{1-x}Fe_xO_{3-\delta}$ perovskites under oxidizing conditions. Solid lines are for visual guidance only.

different configurations in the second coordination sphere around Fe^{3+} give rise to slightly different, unresolved magnetic hyperfine interactions. Note that the IS remains essentially constant for all the sextets in the distribution, thus confirming that all Fe^{3+} cations have the same octahedral coordination. No Fe^{4+} states are detected in the Mössbauer spectra.

In combination with the absence of pentacoordinated Fe^{3+}, the latter observation shows that the charge compensation of Sr^{2+} and A-site cation deficiency in oxidized $(La_{0.75}Sr_{0.25})_{0.95}Cr_{1-x}Fe_xO_{3-\delta}$ occurs via formation of tetravalent chromium cations. The concentration of oxygen vacancies under oxidizing conditions is very low since no traces of iron–oxygen pyramids, easily detectable after reduction (see below), are found. It should be mentioned that Cr^{4+} is frequently observed in Cr-containing perovskite phases [29–31], where surface oxidation and hydration at low temperatures leads even to the formation of Cr^{6+} impurity states. Indeed, thermogravimetric analysis of $(La_{0.75}Sr_{0.25})_{0.95}Cr_{1-x}Fe_xO_{3-\delta}$ revealed very minor weight losses on heating in air (inset in Fig. 5). These variations may originate from surface desorption processes in the intermediate-temperature range and an appearance of modest oxygen deficiency in the bulk at high temperatures. Decreasing chromium concentration leads to smaller mass changes, thus suggesting that the oxygen vacancy formation, if any, is governed by the Cr^{3+}/Cr^{4+} redox couple. However, even neglecting any desorption from $(La_{0.75}Sr_{0.25})_{0.95}Cr_{1-x}Fe_xO_{3-\delta}$ surface, the resultant oxygen nonstoichiometry variations are extremely low, $(6–10)\times10^{-4}$ atoms per formula unit (f.u.). In other words, the crystal lattice of $(La_{0.75}Sr_{0.25})_{0.95}Cr_{1-x}Fe_xO_3$ under oxidizing conditions is oxygen-stoichiometric within the limits of experimental uncertainty. The same conclusion can be drawn from the behavior of Seebeck coefficient in oxidizing atmospheres (Fig. 6). As discussed below, the Seebeck coefficient is proportional to the reciprocal electron–hole concentration and reflects, therefore, any variations in the oxygen deficiency due to the crystal electroneutrality condition. The facts that the thermopower is $p(O_2)$-independent within the limits of experimental error and displays only a very weak increase with temperature, confirm that the oxygen stoichiometry under oxidizing conditions is essentially constant. Finally, one should mention that the observed trends are in excellent agreement with numerous literature data showing that the average oxidation state of chromium cations in Fe- and Cr-containing perovskite solid solutions is always higher than that of iron (e.g., [30,31] and references cited).

3.3. Stability and redox behavior in reducing atmospheres

The room-temperature Mössbauer spectra of reduced $(La_{0.75}Sr_{0.25})_{0.95}Cr_{1-x}Fe_xO_{3-\delta}$, annealed at 1223 K and oxygen partial pressure of 10^{-18} atm (Fig. 4), display three resolved peaks. One of them, at the highest Doppler velocity, has a pronounced shoulder. These spectra were fitted with two quadrupole doublets; introducing additional subspectra did not improve the fitting quality. The IS and quadrupole splitting (QS) values of both doublets (Table 2) indicate that most iron cations still exist in the trivalent state, but oxygen-vacancy formation on reduction leads to the presence of two major coordination numbers, 6 and 5. For the doublet with higher IS, the estimated IS and QS are equal to those of the oxidized phases within the limits of experimental error. This doublet corresponds hence to octahedrally coordinated Fe^{3+}. The lower IS of another subspectrum is characteristic of a lower coordination. The corresponding isomer shifts are significantly higher compared to the range known for tetrahedral coordination in the ferrite-based phases with perovskite-related or brownmillerite structures (0.14–0.21 mm s^{-1}), but are typical for pentacoordinated Fe^{3+} in perovskites [20,26–28,32,33]. Furthermore, this doublet assigned to pentacoordinated Fe^{3+} has higher QS (Table 2), as expected for the sites with more distorted local coordination than octahedral. Hence, the predominant oxidation state of iron in $(La_{0.75}Sr_{0.25})_{0.95}Cr_{1-x}Fe_xO_{3-\delta}$ remains 3+ irrespective of the oxygen partial pressure, while oxygen coordination of Fe^{3+} cations decreases on reduction.

Fig. 7 shows the relative variations of oxygen deficiency on reduction in a dry 10%H_2–90%N_2 flow, calculated from the TGA results (Fig. 5), with respect to the stoichiometry in atmospheric air. The latter reference point was selected as no complete reduction into phase mixtures with definite oxidation states of iron and chromium cations (e.g., metallic Fe) was achieved during TGA experiments up to 1373 K. The results indicate that, although the reduction leads to significant nonstoichiometry values, the overall level of oxygen deficiency can still be tolerated by the perovskite lattice. Taking into account that iron cations are trivalent, and assuming $\delta \approx 0$ in air for the sake of comparison, the estimated average oxidation state of chromium in dry 10%H_2–90%N_2 tends to asymptotically approach +3.10 for $x = 0.3$ and +3.01 for $x = 0.4$ at 1223 K. At 1073 K, these values are +3.16 and +3.14, respectively. Consequently, one may conclude that the redox behavior and electronic conductivity of $(La_{0.75}Sr_{0.25})_{0.95}Cr_{1-x}Fe_xO_{3-\delta}$ should be primarily governed by $Cr^{3+/4+}$ states in the entire $p(O_2)$ range relevant for the electrode applications. In particular, a higher concentration of p-type electronic charge carriers (Cr^{4+}) and higher hole conductivity can be expected for the composition with $x = 0.3$, whereas the Seebeck coefficient should remain positive as for lanthanum–strontium chromites [31]. These trends are indeed observed experimentally (Fig. 8).

Although increasing iron content in $(La_{0.75}Sr_{0.25})_{0.95}Cr_{1-x}Fe_xO_{3-\delta}$ increases reducibility of the materials (Fig. 7), the Mössbauer spectroscopy and thermogravimetric analyses showed no evidence of phase decomposition in mildly reducing atmospheres, as for XRD (Fig. 1). In particular, no traces of metallic iron were detected in the Mössbauer spectra after reduction at 1223 K and $p(O_2) = 10^{-18}$ atm. Taking into account that the low-$p(O_2)$ stability limits of iron-containing phases usually exhibit van't Hoff type dependencies on reciprocal temperature [1,2,34,35], an acceptable thermodynamic stability under anodic conditions in the intermediate-temperature SOFCs can be

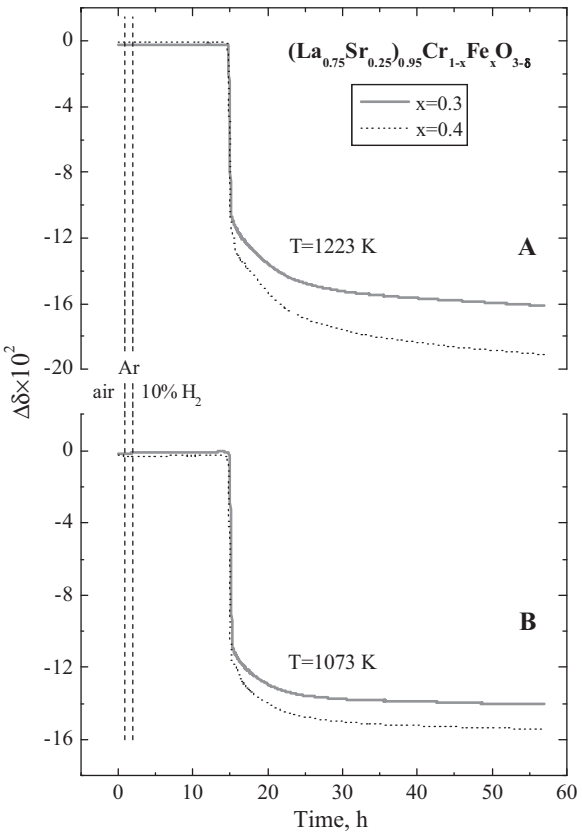

Fig. 7. Variations of the oxygen nonstoichiometry of $(La_{0.75}Sr_{0.25})_{0.95}Cr_{1-x}Fe_xO_{3-\delta}$ on reduction in dry 10%H_2–N_2 gas mixture at 1223 K (A) and 1073 K (B), calculated from thermogravimetric data. The reference points correspond to atmospheric air at a given temperature. The dashed vertical lines show atmosphere changes.

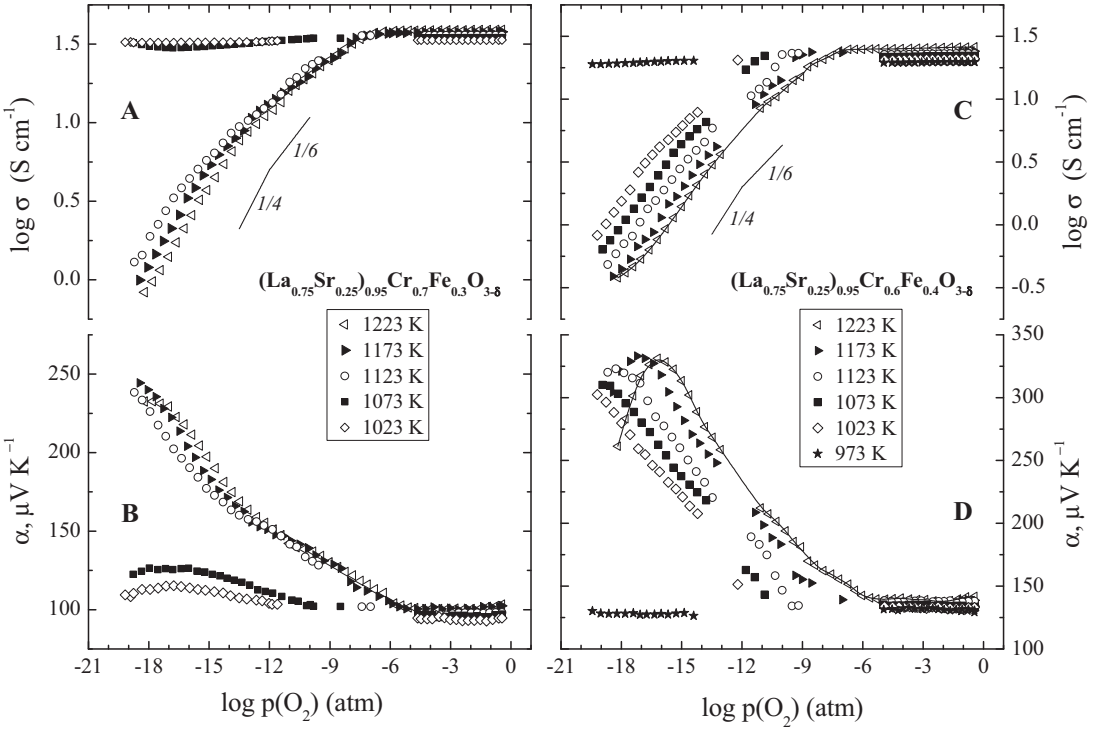

Fig. 8. Oxygen partial pressure dependencies of the total conductivity (A and C) and Seebeck coefficient (B and D) of $(La_{0.75}Sr_{0.25})_{0.95}Cr_{1-x}Fe_xO_{3-\delta}$ ceramics. The data were collected in the isothermal oxidation regime (see text), with equilibration during 2–80 h for each data point. Solid lines are a guide for the eye.

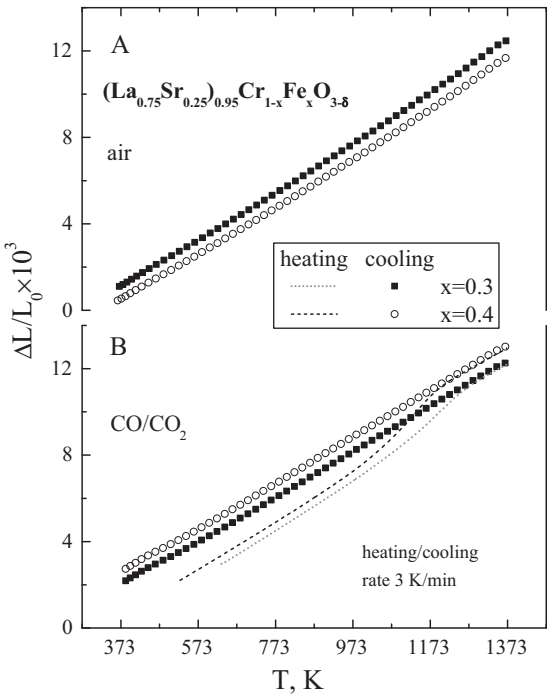

Fig. 9. Dilatometric curves of $(La_{0.75}Sr_{0.25})_{0.95}Cr_{1-x}Fe_xO_{3-\delta}$ ceramics in air (A) and in $CO–CO_2$ atmospheres with $p(O_2) = 3 \times 10^{-20}$ atm at 923 K and 2×10^{-12} atm at 1223 K (B).

expected. Nonetheless, long-term testing is necessary to access reducibility in pure H_2 at 770–970 K.

Another conclusion can be drawn regarding the distribution of oxygen vacancies in the crystal lattice. In a hypothetical state when all chromium cations in reduced $(La_{0.75}Sr_{0.25})_{0.95}Cr_{1-x}Fe_xO_{3-\delta}$ are trivalent as iron, the oxygen vacancy concentration should correspond to approximately 0.19 sites per formula unit ($\delta \approx 0.19$). Assuming a random distribution of the vacancies, approximately 28% penta- and 5% tetra-coordinated B-sites might be predicted. The estimated fractions of pentacoordinated Fe^{3+} (Table 2) are, however, substantially higher, thus indicating a greater energetic favorability for vacancy location near Fe^{3+} in comparison with Cr^{3+}. Moreover, the calculated concentration of pentacoordinated Fe^{3+}, 0.21–0.23 cations/f.u., is almost independent of x and is close to the vacancy concentration. As the oxygen nonstoichiometry is relatively low and statistical distribution of Cr/Fe cations in the B sublattice was confirmed by Rietveld refinement of the XRD patterns, the absence of tetrahedral Fe^{3+} may originate from coulombic repulsion between the randomly distributed oxygen vacancies. No tendency to anion vacancy ordering is hence observed on reduction, in contrast to the perovskite-related systems with higher oxygen deficiency [20,26,27,32]. In the latter cases, extensive vacancy ordering under reducing conditions similar to those used in this work, leads always to an appearance of brownmillerite-like domains and/or to the phase transitions into brownmillerite-type structures. This factor, along with the high concentration of chromium–oxygen polyhedra limiting the chains of iron cations and oxygen vacancies in the perovskite structure, seems responsible for the improved thermodynamic stability of $(La_{0.75}Sr_{0.25})_{0.95}Cr_{1-x}Fe_xO_{3-\delta}$.

3.4. Thermal and chemical expansion

Fig. 9 presents typical dilatometric curves of $(La_{0.75}Sr_{0.25})_{0.95}Cr_{1-x}Fe_xO_{3-\delta}$ ceramics at atmospheric $p(O_2)$ and in flowing $CO–CO_2$ mixture where the oxygen partial pressure, continuously controlled by an electrochemical oxygen sensor, was 3×10^{-20} atm at 923 K and 2×10^{-12} atm at 1223 K. In both cases the thermal expansion is essentially linear up to 1373 K. When pre-oxidized $(La_{0.75}Sr_{0.25})_{0.95}Cr_{1-x}Fe_xO_{3-\delta}$ is heated in $CO–CO_2$ atmosphere, a significant chemical contribution to the apparent thermal expansion is observed at 970–1220 K due to progressive oxygen losses from the perovskite lattice (Fig. 9B). This effect becomes negligible on cooling back in the same atmosphere. The average TECs of $(La_{0.75}Sr_{0.25})_{0.95}Cr_{1-x}Fe_xO_{3-\delta}$ are relatively low, $10.3–11.3 \times 10^{-6}\ K^{-1}$, and tend to slightly decrease on reduction (Table 1). These TECs are substantially lower compared to other Fe-containing perovskites (e.g., [36]) due to the stabilization of Fe^{3+} state, validated by the Mössbauer spectroscopy. The moderate thermal expansion provides an acceptable thermomechanical compatibility of $(La_{0.75}Sr_{0.25})_{0.95}Cr_{1-x}Fe_xO_{3-\delta}$ and common solid electrolytes, such as yttria-stabilized zirconia (YSZ), CGO and LSGM [7].

Table 3
Relative isothermal expansion of $(La_{0.75}Sr_{0.25})_{0.95}Cr_{1-x}Fe_xO_{3-\delta}$ ceramics on reduction.

x	T, K	$p(O_2)$, atm	$(L - L_{air})/L_{air} \times 10^3$
0.3	923	3.0×10^{-20}	7.6
	973	1.3×10^{-18}	8.1
	1023	4.0×10^{-17}	8.7
	1073	8.9×10^{-16}	9.2
	1123	1.5×10^{-14}	9.7
	1173	2.0×10^{-13}	10.3
	1223	2.1×10^{-12}	10.8
0.4	923	3.0×10^{-20}	8.3
	973	1.3×10^{-18}	8.8
	1023	4.0×10^{-17}	9.4
	1073	8.9×10^{-16}	9.9
	1123	1.5×10^{-14}	10.5
	1173	2.0×10^{-13}	11.0
	1223	2.1×10^{-12}	11.5

Despite the Fe^{3+} stabilization, the isothermal chemical strains of $(La_{0.75}Sr_{0.25})_{0.95}Cr_{1-x}Fe_xO_{3-\delta}$ measured by dilatometry (Table 3) are 3–5 times higher compared to $(La_{0.75}Sr_{0.25})_{0.95}Cr_{0.5}Mn_{0.5}O_{3-\delta}$ under similar conditions [12]. The overall level of chemical expansion observed for $(La_{0.75}Sr_{0.25})_{0.95}Cr_{1-x}Fe_xO_{3-\delta}$, is intermediate between the perovskite-type chromites [37,38] and ferrites [39,40]. This fact, and increasing volume variations when x increases (Table 2), are in agreement with the above conclusion that iron additions promote reducibility of $(La_{0.75}Sr_{0.25})_{0.95}Cr_{1-x}Fe_xO_{3-\delta}$. Note that the apparent lattice expansivity may also be contributed by the "rhombohedral → orthorhombic" phase transition on reduction. Whatever the microscopic mechanisms, the thermomechanical stability of the title materials on redox cycling is worse with respect to LSCM.

3.5. Oxygen permeability and ionic conductivity

Fig. 10 displays the steady-state oxygen permeation fluxes (j) through dense $(La_{0.75}Sr_{0.25})_{0.95}Cr_{1-x}Fe_xO_{3-\delta}$ membranes of different thickness (d) under air/H_2–H_2O–N_2 gradients, and the specific oxygen permeability $J(O_2)$ related to these quantities as ([14,21,31] and references therein):

$$j = \frac{J(O_2)}{d} \cdot \left(\ln \frac{p_2}{p_1}\right) \quad (1)$$

where p_2 and p_1 are the feed- and permeate-side oxygen partial pressures, respectively. When the oxygen chemical potential gradient is high enough, increasing membrane thickness leads to lower oxygen fluxes, whereas the specific permeability proportional to $j \times d$ becomes thickness-independent within the limits of experimental error. In combination with relatively high total conductivity

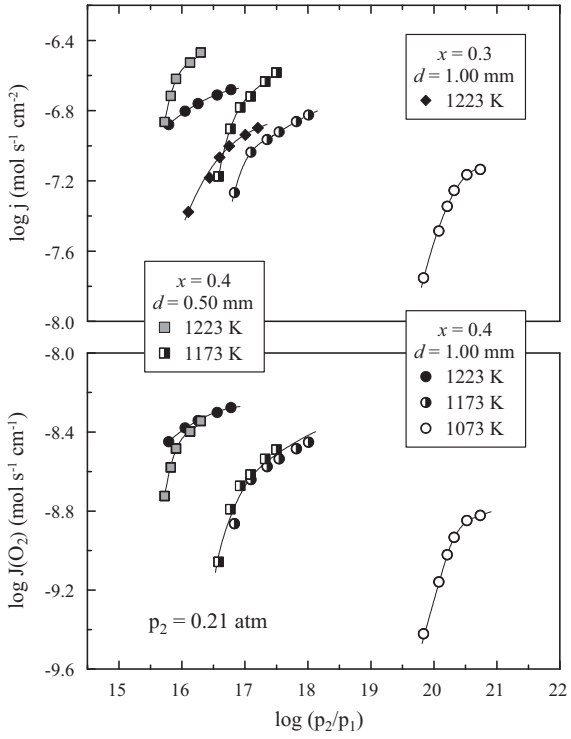

Fig. 10. Oxygen permeation fluxes (top) and specific oxygen permeability (bottom) of $(La_{0.75}Sr_{0.25})_{0.95}Cr_{1-x}Fe_xO_{3-\delta}$ ceramics under air/H_2–H_2O–N_2 gradient. Solid lines are a guide for the eye.

(Fig. 8), this behavior unambiguously indicates that the permeation is limited by the bulk ion diffusion, and makes it possible to estimate the partial ionic conductivity (σ_O) in reducing atmospheres [2]:

$$\sigma_O(p_1) = \frac{16F^2 d}{RT} \cdot \left(\frac{\partial j}{\partial[\ln p_1]} \right)_{p_2} \quad (2)$$

where F, R and T are the Faraday constant, universal gas constant and absolute temperature, respectively. When the oxygen chemical potential gradient decreases, the permeability starts to depend on the membrane thickness, thus indicating an increasing role of the surface exchange and/or gas diffusion limitations. The values of ionic conductivity and ion transference numbers ($t_O = \sigma_O/\sigma$) estimated by Eq. (2) at 1223 K and $p_1 = 10^{-17}$ atm, are presented in Table 4. As for the oxygen permeation fluxes (Fig. 10), the bulk ionic transport in the title perovskites increases with x due to increasing oxygen vacancy concentration in reducing atmospheres and weakening of the metal—oxygen bonds. Due to the same reasons, the ionic conductivity of $(La_{0.75}Sr_{0.25})_{0.95}Cr_{1-x}Fe_xO_{3-\delta}$ is higher with respect to acceptor-doped lanthanum chromites [41] and LSCM [12], but is slightly lower compared to (La,Sr)$FeO_{3-\delta}$ with similar strontium concentrations [42].

3.6. p-Type electronic conductivity and Seebeck coefficient

Under oxidizing conditions the total conductivity of $(La_{0.75}Sr_{0.25})_{0.95}Cr_{1-x}Fe_xO_{3-\delta}$ (Fig. 11) is comparable to that of other oxide electrode materials considered for the "symmetrical" SOFC/SOEC concept where the cathode and anode are made of similar compositions, such as LSCM [3,7]. The thermopower sign and oxygen permeation data (Figs. 6, 8 and 10) show that the conductivity is predominantly p-type electronic in the entire $p(O_2)$ range studied in this work, as for most acceptor-doped phases based on $LaCrO_3$ [31]. Increasing iron content leads to

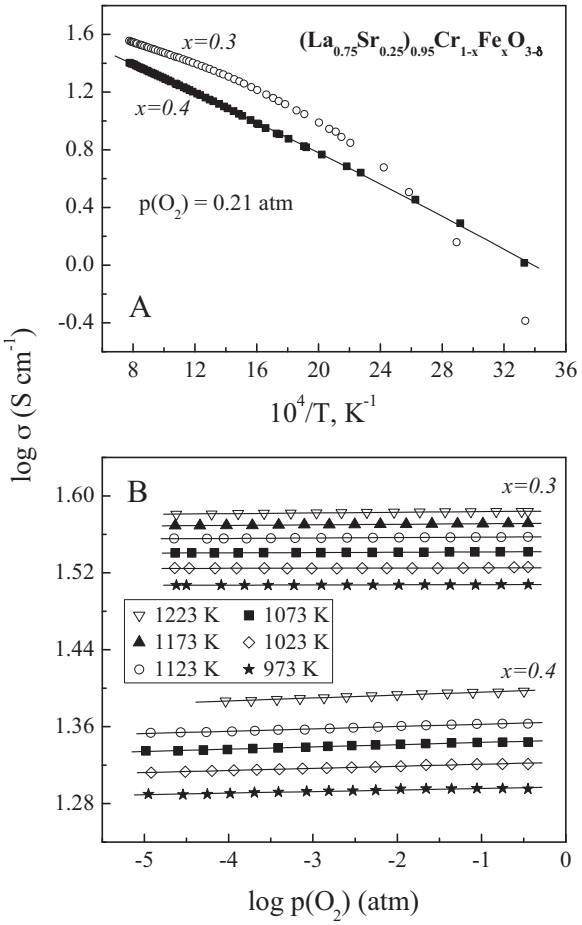

Fig. 11. Total conductivity of $(La_{0.75}Sr_{0.25})_{0.95}Cr_{1-x}Fe_xO_{3-\delta}$ ceramics as a function of temperature in air (A) and oxygen partial pressure under oxidizing conditions (B).

lower hole conduction, primarily due to lowering charge-carrier concentration. As the oxygen nonstoichiometry variations in oxidizing atmospheres are very minor (Fig. 5), the conductivity and Seebeck coefficient in these conditions are essentially independent of the oxygen pressure (Figs. 6 and 11B). Reducing $p(O_2)$ results in progressive oxygen losses from the perovskite lattice and in decreasing Cr^{4+} concentration, which is reflected by lower conductivity and higher thermopower (Fig. 8). This mechanism implies a small-polaron hopping mechanism as for other perovskite-type chromites [31]. Although exact calculations of the charge-carrier concentration (p) and mobility (μ_p) are impossible in the present case due to a variety of likely spin-degeneracy and site-exclusion effects influencing the number of states (N), their temperature dependencies in a narrow $p(O_2)$ range can be evaluated from the Seebeck coefficient and conductivity data by using the modified Heikes equation [35,43]:

$$\alpha = \frac{k}{e} \cdot \ln \frac{\beta N - p}{p} \quad (3)$$

$$\sigma = \frac{\mu_p \cdot e \cdot p \cdot N_{fu}}{V_{uc}} \quad (4)$$

where N and p are related to unit formula, N_{fu} is the number of formula units per unit cell, V_{uc} is the unit-cell volume, and β is a constant. The results of these estimations (Fig. 12) indicate, first of all, that the hole mobility is thermally activated. This fact and the relatively low mobility level both provide evidence in favor of the small-polaron mechanism, in agreement with the conductivity activation energies (Table 1). Second, the μ_p values tend to decrease

Table 4
Partial oxygen–ionic conductivity and ion transference numbers of $(La_{0.75}Sr_{0.25})_{0.95}Cr_{1-x}Fe_xO_{3-\delta}$ at $T = 1223$ K and $p(O_2) = 10^{-17}$ atm, calculated from the oxygen permeability and total conductivity data.

x	Total conductivity σ, S cm^{-1}	Ionic conductivity σ_O, S cm^{-1}	Transference numbers t_O
0.3	1.41	0.056	0.040
0.4	0.54	0.079	0.15

with increasing x, suggesting that the iron cations are essentially excluded from the hole migration processes.

Fig. 13 illustrates another important trend revealed in the course of the electrical measurements, namely, strong hysteresis phenomena on redox cycling in moderately reducing atmospheres. The corresponding $p(O_2)$ range extends down to substantially lower oxygen chemical potentials than those known for the experimental problems, associated with stagnated diffusion and equilibration processes involving gaseous oxygen-containing species (e.g., [42]). At 973–1273 K the sluggish equilibration kinetics and resultant experimental uncertainties are usually observed at the oxygen partial pressures from 10^{-5}–10^{-4} atm down to 10^{-11}–10^{-8} atm, depending on temperature. In the present case, the low-$p(O_2)$ limit of the nonequilibrium plateau-like behavior indicative of "frozen" oxygen stoichiometry on reduction (Fig. 13) varied from 10^{-14} down to 10^{-20} atm at 1023–1223 K, although the time used for equilibrating was up to 80 h. Notice that a significantly faster equilibration and a good reproducibility of the electrical properties were observed beyond the plateaus. Consequently, only the data collected in the oxidation regime (Fig. 8) were considered as equilibrium, except for 973–1073 K when the oxygen content seems to be essentially frozen in the entire $p(O_2)$ range. The hysteresis phenomena may originate either from the perovskite phase transition or from large differences in the oxygen exchange kinetics on reduction and on oxidation. Whatever the microscopic mechanisms, the slow reduction kinetics makes it possible to increase electronic conductivity of $(La_{0.75}Sr_{0.25})_{0.95}Cr_{1-x}Fe_xO_{3-\delta}$ electrodes under intermediate-temperature SOFC anodic conditions by periodic current pulses.

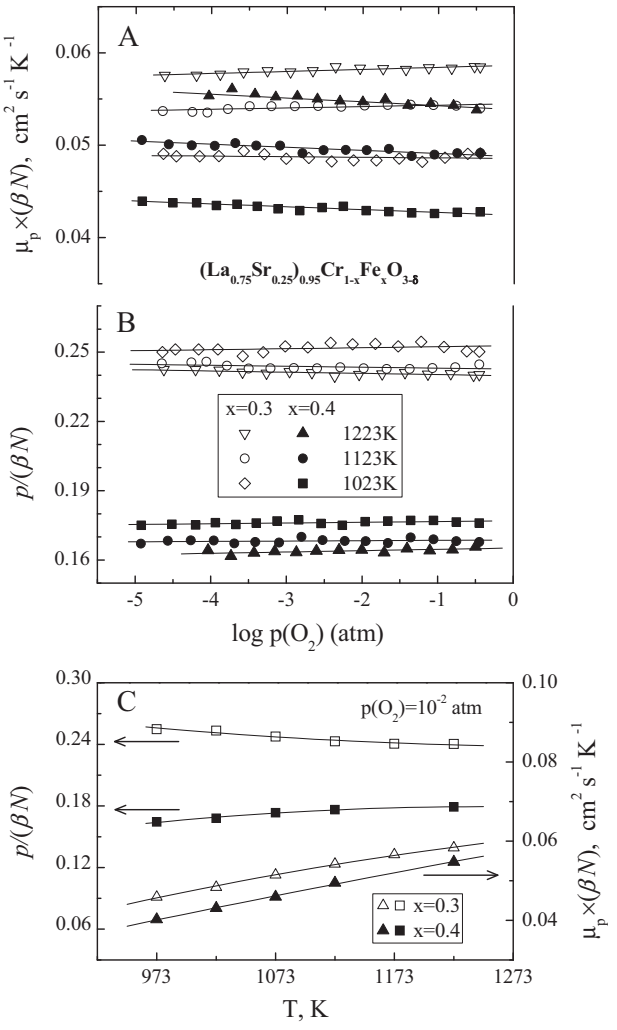

Fig. 12. Oxygen partial pressure dependencies of the normalized hole mobility (A) and $p/(\beta N)$ ratio (B) calculated from the conductivity and Seebeck coefficient data at 1023–1223 K, and temperature dependencies of these parameters at $p(O_2) = 10^{-2}$ atm (C). Solid lines are a guide for the eye.

3.7. Anodic performance

Typical anodic polarization curves of porous $(La_{0.75}Sr_{0.25})_{0.95}Cr_{1-x}Fe_xO_{3-\delta}$ electrodes with CGO interlayers applied onto LSGM solid electrolyte are presented in Fig. 14. Table 5 compares their electrochemical performance with other anode compositions, including LSCM [12] and $(La,Sr)(Ti,Cr,Mn)O_{3-\delta}$ perovskites [14]. All the data were collected in the electrochemical cells with similar electrode thicknesses and geometry described elsewhere [12], using identical Pt gauze current collectors, in flowing 10%H_2–90%N_2 gas mixture humidified at room temperature. The electrochemical activity of $(La_{0.75}Sr_{0.25})_{0.95}Cr_{1-x}Fe_xO_{3-\delta}$ tends to moderately decrease with increasing x, in correlation with the electronic conductivity variations. The opposite trends observed for the oxygen permeability and ionic conductivity (Fig. 10 and Table 4) confirm previous conclusion [12] that the impact of ionic transport is much smaller with respect to electronic, probably due to the presence of ceria interlayers and/or overall low level of the ion diffusivity. These factors make it possible to increase the electrode performance via infiltration of $CeO_{2-\delta}$, which is a mixed ionic–electronic conductor under anodic conditions. On the other hand, the electrode resistivity variations with composition (Table 5) cannot be simply ascribed to the only limiting effect of electron transfer, and indicate also non-negligible contributions

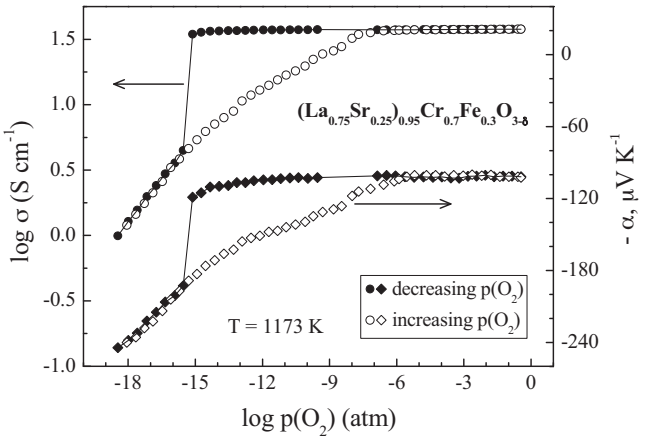

Fig. 13. One example of the hysteresis behavior of the electrical properties of $(La_{0.75}Sr_{0.25})_{0.95}Cr_{0.7}Fe_{0.3}O_{3-\delta}$ on redox cycling.

Table 5
Comparison of the total conductivity[a] and electrochemical performance[b] of various perovskite-type oxide anode materials.

Composition	σ, S cm^{-1}	Surface modification	η, mV	R_η, Ω cm^2	Activation energy for area-specific electrode conductivity		Reference
					T, K	E_a, kJ mol^{-1}	
$(La_{0.75}Sr_{0.25})_{0.95}Cr_{0.7}Fe_{0.3}O_{3-\delta}$	1.8	–	35	1.2	873–1073	71	This work
$(La_{0.75}Sr_{0.25})_{0.95}Cr_{0.6}Fe_{0.4}O_{3-\delta}$	0.7	–	44	1.6	873–1073	90	This work
$(La_{0.75}Sr_{0.25})_{0.95}Cr_{0.5}Mn_{0.5}O_{3-\delta}$	2.3	–	73	2.8	973–1073	66	[12]
		$CeO_{2-\delta}$	36	1.3	973–1073	87	
$(La_{0.55}Sr_{0.45})_{0.95}Cr_{0.3}Mn_{0.5}Ti_{0.2}O_{3-\delta}$		–	154	4.7	973–1073	96	[14]
$La_{0.5}Sr_{0.5}Mn_{0.5}Ti_{0.5}O_{3-\delta}$	1.7	–	54	2.1	873–1073	55	

[a] The data on total conductivity (σ) correspond to T = 1123 K and $p(O_2) = 10^{-18}$ atm.
[b] η the anodic overpotential at the current density of 30 mA cm^{-2} and 1073 K, in flowing humidified 10%H_2–90%N_2. R_η is the area-specific polarization resistance under open-circuit conditions in the same atmosphere.

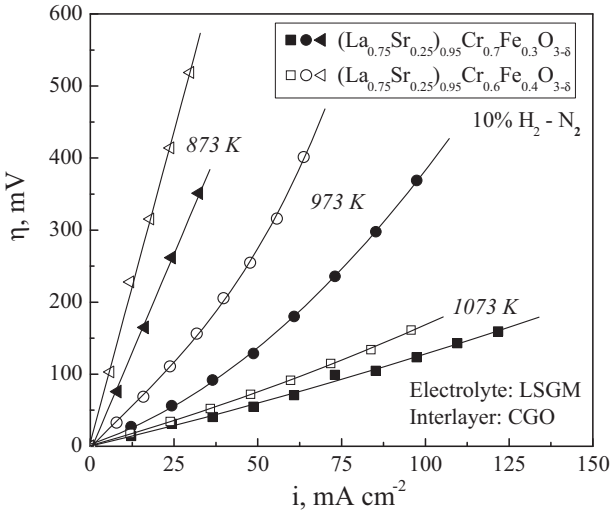

Fig. 14. Anodic polarization curves of porous $(La_{0.75}Sr_{0.25})_{0.95}Cr_{1-x}Fe_xO_{3-\delta}$ electrodes with CGO interlayers deposited onto LSGM solid electrolyte, in humidified 10%H_2–90%N_2 atmosphere at 873–1073 K.

of other factors, such as metal—oxygen bonding energy affecting oxygen exchange kinetics [7]. For instance, the polarization resistance of $(La_{0.75}Sr_{0.25})_{0.95}Cr_{0.7}Fe_{0.3}O_{3-\delta}$ is lower than that of $(La_{0.75}Sr_{0.25})_{0.95}Cr_{0.5}Mn_{0.5}O_{3-\delta}$, although the electronic conductivity of LSCM is higher.

4. Conclusions

The Mössbauer spectroscopy and thermogravimetric studies combined with electrical measurements show that the incorporation of moderate amounts of iron into acceptor-doped $LaCrO_3$ enable to stabilize Fe^{3+} states in a wide $p(O_2)$ range necessary for the intermediate-temperature electrochemical applications. Perovskite-type $(La,Sr)(Cr,Fe)O_{3-\delta}$ exhibit moderate TECs compatible with common solid-electrolyte materials, relatively low oxygen-stoichiometry variations, and substantially high oxygen permeability and ionic conduction in reducing atmospheres. These perovskites possess also a higher electrochemical activity under anodic conditions and lower costs compared to LSCM. At the same time, a number of functional properties of $(La,Sr)(Cr,Fe)O_{3-\delta}$, primarily electronic conductivity at low $p(O_2)$ and chemical expansivity, are worse with respect to their Mn-containing analogs. When iron concentration increases, these disadvantages become more pronounced. Namely, the electronic conductivity decreases with increasing x in $(La_{0.75}Sr_{0.25})_{0.95}Cr_{1-x}Fe_xO_{3-\delta}$, while the polarization resistance, reducibility and chemical expansion tend to increase. The developments of new electrode compositions require, therefore, an optimization of Cr:Fe concentration ratio in the range $0.1 \le x \le 0.3$, and infiltration of catalytically active additives with significant mixed conductivity, such as doped ceria or $CeVO_{3\pm\delta}$.

Acknowledgements

This work was partially supported by the FCT, Portugal (projects PTDC/CTM/64357/2006, PTDC/CTM-CER/114561/2009, SFRH/BPD/28629/2006 and SFRH/BD/45227/2008), and by the Ministry of Education and Science of the Russian Federation (state contract 02.740.11.5214).

References

[1] Fuel Cell Handbook, 7th edition, EG&G Technical Services, Morgantown, West Virginia, 2004.
[2] V. Kharton (Ed.), Solid State Electrochemistry. I. Fundamentals, Materials and their Applications, Wiley-VCH, Weinheim, 2009.
[3] S. Tao, J.T.S. Irvine, Nat. Mater. 2 (2003) 320.
[4] J. Peña-Martínez, D. Marrero-López, D. Pérez-Coll, J.C. Ruiz-Morales, P. Núñez, Electrochim. Acta 52 (2007) 2950.
[5] J.M. Haag, B.D. Madsen, S.A. Barnett, K.R. Poeppelmeier, Electrochem. Solid State Lett. 11 (2008) B51.
[6] J. Sfeir, J. Power Sources 118 (2003) 276.
[7] E.V. Tsipis, V.V. Kharton, J. Solid State Electrochem. 12 (2008) 1039; E.V. Tsipis, V.V. Kharton, J. Solid State Electrochem. 15 (2011) 1007.
[8] S. Primdahl, J.R. Hansen, L. Grahl-Madsen, P.H. Larsen, J. Electrochem. Soc. 148 (2001) A74.
[9] O.A. Marina, N.L. Canfield, J.W. Stevenson, Solid State Ionics 149 (2002) 21.
[10] X.J. Chen, Q.L. Liu, K.A. Khor, S.H. Chan, J. Power Sources 165 (2007) 34.
[11] J. Wan, J.H. Zhu, J.B. Goodenough, Solid State Ionics 177 (2006) 1211.
[12] V.V. Kharton, E.V. Tsipis, I.P. Marozau, A.P. Viskup, J.R. Frade, J.T.S. Irvine, Solid State Ionics 178 (2007) 101.
[13] M. Oishi, K. Yashiro, K. Sato, J. Mizusaki, T. Kawada, J. Solid State Chem. 181 (2008) 3177.
[14] V.A. Kolotygin, E.V. Tsipis, A.L. Shaula, E.N. Naumovich, J.R. Frade, S. Bredikhin, V.V. Kharton, J. Solid State Electrochem. 15 (2011) 313.
[15] L.A. Chick, L.R. Pederson, G.D. Maupin, J.L. Bates, L.E. Thomas, G.J. Exarhos, Mater. Lett. 10 (1990) 6.
[16] M.V. Patrakeev, E.B. Mitberg, A.A. Lakhtin, I.A. Leonidov, V.L. Kozhevnikov, V.V. Kharton, M. Avdeev, F.M.B. Marques, J. Solid State Chem. 167 (2002) 203.
[17] V.V. Kharton, A.A. Yaremchenko, E.V. Tsipis, A.A. Valente, M.V. Patrakeev, A.L. Shaula, J.R. Frade, J. Rocha, Appl. Catal. A 261 (2004) 25.
[18] V.V. Kharton, A.V. Kovalevsky, M. Avdeev, E.V. Tsipis, M.V. Patrakeev, A.A. Yaremchenko, E.N. Naumovich, J.R. Frade, Chem. Mater. 19 (2007) 2027.
[19] V.V. Kharton, A.L. Shaula, N.P. Vyshatko, F.M.B. Marques, Electrochim. Acta 48 (2003) 1817.
[20] J.C. Waerenborgh, D.P. Rojas, N.P. Vyshatko, A.L. Shaula, V.V. Kharton, I.P. Marozau, E.N. Naumovich, Mater. Lett. 57 (2003) 4388.
[21] A.A. Yaremchenko, V.V. Kharton, A.P. Viskup, E.N. Naumovich, N.M. Lapchuk, V.N. Tikhonovich, J. Solid State Chem. 142 (1999) 325.
[22] J. Hesse, A. Rübartsch, J. Phys. E 7 (1974) 526.
[23] V.L. Kozhevnikov, I.A. Leonidov, J.A. Bahteeva, M.V. Patrakeev, E.B. Mitberg, K.R. Poeppelmeier, Chem. Mater. 16 (2004) 5014.
[24] S. Tao, J.T.S. Irvine, Chem. Mater. 16 (2004) 4116.
[25] R.D. Shannon, Acta Crystallogr. A 32 (1976) 751.
[26] P. Adler, U. Schwarz, K. Syassen, A.P. Milner, M.P. Pasternak, M. Hanfland, J. Solid State Chem. 155 (2000) 381.
[27] P.D. Battle, T.C. Gibb, S. Nixon, J. Solid State Chem. 73 (1988) 330.
[28] P.D. Battle, T.C. Gibb, S. Nixon, J. Solid State Chem. 79 (1989) 86.

[29] K. Rida, A. Benabbas, F. Bouremmad, M.A. Peña, E. Sastre, A. Martínez-Arias, Appl. Catal. B 84 (2008) 457.
[30] M.D. Carvalho, T. Ramos, L.P. Ferreira, A. Wattiaux, Solid State Sci. 12 (2010) 476.
[31] V.V. Kharton, A.A. Yaremchenko, E.N. Naumovich, J. Solid State Electrochem. 3 (1999) 303.
[32] V.V. Kharton, M.V. Patrakeev, J.C. Waerenborgh, V.A. Sobyanin, S.A. Veniaminov, A.A. Yaremchenko, P. Gaczyński, V.D. Belyaev, G.L. Semin, J.R. Frade, Solid State Sci. 7 (2005) 1344.
[33] V.V. Kharton, A.V. Kovalevsky, M.V. Patrakeev, E.V. Tsipis, A.P. Viskup, V.A. Kolotygin, A.A. Yaremchenko, A.L. Shaula, E.A. Kiselev, J.C. Waerenborgh, Chem. Mater. 20 (2008) 6457.
[34] J. Mizusaki, Solid State Ionics 52 (1992) 79.
[35] P. Kofstad, Nonstoichiometry Diffusion and Electrical Conductivity in Binary Metal Oxides, Wiley-Interscience, New York, 1972.
[36] E.V. Tsipis, V.V. Kharton, J. Solid State Electrochem. 12 (2008) 1367.
[37] A. Atkinson, T.M.G.M. Ramos, Solid State Ionics 129 (2000) 259.
[38] A. Zuev, L. Singheiser, K. Hilpert, Solid State Ionics 147 (2002) 1.
[39] V.V. Kharton, A.A. Yaremchenko, M.V. Patrakeev, E.N. Naumovich, F.M.B. Marques, J. Eur. Ceram. Soc. 23 (2003) 1417.
[40] A. Fossdal, M. Menon, I. Wærnhus, K. Wiik, M.-A. Einarsrud, T. Grande, J. Am. Ceram. Soc. 87 (2004) 1952.
[41] D.-K. Lee, H.-I. Yoo, J. Electrochem. Soc. 147 (2000) 2835.
[42] J.A. Bahteeva, I.A. Leonidov, M.V. Patrakeev, E.B. Mitberg, V.L. Kozhevnikov, K.R. Poeppelmeier, J. Solid State Electrochem. 8 (2004) 578.
[43] J.-P. Doumerc, J. Solid State Chem. 110 (1994) 419.